Mesoscopic Architectures Made of Electrically Charged Binary Colloidal Nanosheets in Aqueous System

Mesoscopic Architectures Made of Electrically Charged Binary Colloidal Nanosheets in Aqueous System

Teruyuki Nakato,*[1,2] Atsushi Takahashi,[3] Shinya Terada,[1] Shogo Yamaguchi,[1] Emiko Mouri,[1,2] Morio Shintate,[4] Shinya Yamamoto,[4] Yusuke Yamauchi,[5,6,7] and Nobuyoshi Miyamoto*[4]

[1] Department of Applied Chemistry, Kyushu Institute of Technology, 1-1 Sensui-cho, Tobata, Kitakyushu, Fukuoka 804-8550, Japan

[2] Strategic Research Unit for Innovative Multiscale Materials, Kyushu Institute of Technology, 1-1 Sensui-cho, Tobata, Kitakyushu, Fukuoka 804-8550, Japan

[3] Graduate School of Bio-Applications and Systems Engineering, Tokyo University of Agriculture and Technology, 2-24-16 Naka-cho, Koganei, Tokyo 184-8588, Japan

[4] Department of Life, Environment, and Applied Chemistry, Faculty of Engineering, Fukuoka Institute of Technology, 3-30-1 Wajiro-higashi, Higashi-ku, Fukuoka 811-0295, Japan

[5] School of Chemical Engineering and Australian Institute for Bioengineering and Nanotechnology (AIBN), The University of Queensland, Brisbane, QLD 4072, Australia

[6] Department of Plant & Environmental New Resources, Kyung Hee University, 1732 Deogyeong-daero, Giheunggu, Yongin-si, Gyeonggi-do 446-701, South Korea

[7] International Research Center for Materials Nanoarchitectonics (WPI-MANA), National Institute for Materials Science (NIMS), 1-1 Namiki, Tsukuba, Ibaraki 305-0044, Japan

Abstract

Inorganic layered materials can be converted to colloidal liquid crystals through exfoliation into inorganic nanosheets, and binary nanosheet colloids exhibit rich phase behavior characterized by multiphase coexistence. In particular, niobate–clay binary nanosheet colloids are characterized by phase separation at a mesoscopic (~ several tens of micrometers) scale whereas they are apparently homogeneous at a macroscopic scale. Although the mesoscopic structure of the niobate–clay binary colloid is advantageous to realize unusual photochemical functions, the structure itself has not been clearly demonstrated in real space. The present study investigated the structure of niobate–clay binary nanosheet colloids in detail. Four clay nanosheets (hectorite, saponite, fluorohectorite, and tetrasilisic mica) with different lateral sizes were compared. Small-angle X-ray scattering (SAXS) indicated lamellar ordering of niobate nanosheets in the binary colloid. The basal spacing of the lamellar phase was reduced by increasing the concentration of clay nanosheets, indicating the compression of the liquid crystalline niobate phase by the isotropic clay phase. Scattering and fluorescence microscope observations using confocal laser scanning microscopy (CLSM) demonstrated the phase separation of niobate and clay nanosheets in real space. Niobate nanosheets assembled into domains of several tens of micrometers whereas clay nanosheets were located in voids between the niobate domains. The results clearly confirmed the spatial separation of two nanosheets and the phase separation at a mesoscopic scale. Distribution of clay nanosheets is dependent of the employed clay nanosheets; the nanosheets with large lateral length are more localized or assembled. This is in harmony with larger basal spacings of niobate lamellar phase for large clay particles. Although three-dimensional compression of the niobate phase by the coexisting clay phase was observed at low clay

concentrations, the basal spacing of niobate phase was almost constant irrespective of niobate concentrations at high clay concentrations, which was ascribed to competition of compression by clay phase and restoring of the niobate phase.

INTRODUCTION

Multicomponent systems show rich phase behavior to form various multiphase coexisting structures. Appropriate designs of structural and functional interactions between the components can develop novel advanced materials. In particular, mesoscopic multiphase structures, where individual phases coexisting at mesoscopic scales from micrometers to sub-millimeters are assembled into a macroscopic structure, play crucial roles in realizing advanced functions of a broad range of materials from living things[1] to ceramic[2] and steel.[3] In addition, mesoscopic multiphase structures of living things are characterized by dynamic properties, by which energy, electron, and mass transfers are controlled by external stimuli.[4] Thus, multiphasic and dynamic organizations of mesoscale components provide a broad range of hierarchical structures applicable to artificial organs, microrobots, micromachines, and so forth. However, previously developed examples are assembled with organic building blocks in most cases. Organization of dynamic mesoscopic multiphase structures with inorganic building blocks will enable unusual advanced materials by cooperation of specific structural, electronic, optic, and magnetic properties of inorganic species with dynamic control of their functions.

Multicomponent inorganic colloids are typical but still undeveloped examples of dynamic hierarchical multiphase systems constructed by inorganic particles.[5, 6]

Multicomponent colloids consisting of morphologically different particles generally cause phase separation when attractive interactions are absent among particles. This is basically understood by entropically driven demixing called depletion.[7-9] When multicomponent colloids contain anisotropic particles, shape anisotropy of the particles add liquid crystallinity to the systems, as explained by the entropically driven phase transition established by Onsager.[10, 11] With these mechanisms, binary systems with low-dimensional particles exemplified by plate–sphere and plate–rod mixtures show multiphase coexistence involving liquid crystalline phases.[12-16] However, limited experimentally verified systems have been reported in particular for aqueous systems.[17-20]

For aqueous plate–plate binary colloids, electrically charged inorganic nanosheets prepared by exfoliation of inorganic layered crystals have been developed in the past decades. Phase behavior of nanosheet colloids is characterized by stable LC phases due to highly anisotropic shape of nanosheets with 1-nm thickness and micrometer-level lateral size.[21, 22] Examples are nanosheet colloids of metal phosphates, layered niobates and titanates, clay minerals, graphene oxides, and layered metal carbides (MXenes).[21-28] Mixing of two nanosheets without attractive interactions causes phase separation to evolve multiphase coexistence of LC and isotropic phases, as evidenced by titanate–clay binary nanosheet colloids, where both the nanosheets are negatively charged.[29-31] However, phase separation of multicomponent colloids is usually obtained at eye-detectable macroscopic scales.[32-34] In fact, the titanate–clay binary colloids exhibit multiphase coexistence at a macroscopic scale.[30] Only a very few papers have reported suppression of macroscopic separation by glass formation.[35, 36]

In contrast, we have succeeded in organizing a mesoscopic multiphase

coexistence by using an aqueous binary colloidal system of negatively charged niobate (designated as NB hereafter) and smectite-type clay nanosheets.[29] In this system, although both of the inorganic nanosheets with a thickness of ca. 1 nm and lateral length up to several micrometers are mixed and apparently homogeneously dispersed at a macroscopic (naked eye) scale, they are phase-separated at a mesoscopic scale. However, this system is not in a glass state but fluid. The dynamic nature allows particle diffusion in the colloid to achieve controllable photoinduced electron transfer, accumulation, and photocatalytic reactions between photocatalytically active NB nanosheets and electron-accepting molecules loaded on clay particles.[37-40] Thus, our NB–clay binary colloid is a rare example of hierarchically organized multicomponent photofunctional inorganic liquid crystalline colloid with mesoscopic multiphase structures retaining high fluidity of particles.[29, 37] Although each phase is held at a mesoscopic scale to work as a dynamic functional unit, the whole structure of NB–clay binary system has only been qualitatively characterized by spectroscopic and small-angle neutron scattering measurements.

In the present study, we clarify the real-space structure of NB–clay binary nanosheet colloids by small-angle X-ray scattering (SAXS) and confocal laser scanning microscopy (CLSM). Their colloidal structure is characterized by the coexistence of liquid crystalline NB and isotropic clay nanosheets. The NB nanosheets are present as liquid crystalline domains of mesoscopic scale (~ 10 μm), suffering from compression by coexisting clay nanosheets, as illustrated in Scheme 1. Such mesoscopic dynamic colloidal architecture is independent of clay particles even though their size is different by two orders of magnitude, although the distribution of clay nanosheets is somewhat different with the clay source. Our systematic study can open up a new paradigm for designing and understanding new colloidal systems made of various nanosheets.

EXPERIMENTAL SECTION

Materials. NB–clay aqueous binary nanosheet colloids were prepared by simply mixing aqueous colloids of NB and clay nanosheets. Milli-Q water was used in all of the samples. NB nanosheet colloids were obtained from potassium hexaniobate crystallites ($K_4Nb_6O_{17}$) through exfoliation using propylammonium ions as the exfoliating reagent.[21] $K_4Nb_6O_{17}$ single crystals (~ 5 mm size, 1.5 g) were dispersed in an aqueous propylammonium chloride solution (0.2 mol L^{-1}, 87 mL) and heated at 80 °C for 7 d. Solid component recovered by centrifugation was dispersed and stirred in water, and centrifuged again. The dispersion–centrifugation process was repeated twice. Then, the solid product was dispersed in water and dialyzed against water (5 h, 5 times and 24 h, twice). With this procedure, we reproducibly obtained niobate nanosheets with lateral particle size of around 2 μm.

Smectite-type clay minerals were dispersed in water to yield clay colloids. We examined four synthetic clay minerals: hectorite (Laponite RD, Rockwood Additives Ltd.), saponite (Sumecton SA, Kunimine Industries Co.), fluorohectorite (NHT sol, Topy Industries Co.), and fluorotetrasilisic mica (NTS-5, Topy Industries Co.). Among them, two clay minerals (hectorite and saponite, written as Hect and Sapo, respectively) received as powder samples were dispersed in water without further purification to obtain colloid samples. Both of Hect and Sapo nanosheets have about 30 nm of lateral length (diameter).[41, 42] The other two clays (fluorohectorite and tetrasilisic mica, indicated as FH and TSM, respectively) were received as aqueous suspensions. They were centrifuged, by which the clay suspensions were separated into three phases: upper supernatant, intermediate viscous sol, and lower sediment phases.[23] The sol phase was

picked up and dialyzed with water, and then dried at 60 °C. Lateral particle sizes of FH and TSM were 1-2 μm,[23] being larger than Hect and Sapo by two orders of magnitude, while all of the clay nanosheets possessed the same thickness.

SAXS Measurements. All of the samples were subjected to SAXS measurements. They were performed on a Rigaku NANO-Viewer apparatus (CuKα radiation, 40 kV, 30 mA) having the accessible q range from 0.1 to 1 nm^{-1}. Hereafter, q denotes the magnitude of scattering vector defined by $q = [4\pi \sin(\theta/2)]/\lambda$, where θ and λ are the scattering angle and wavelength of the X-ray beam (0.15418 nm), respectively. For the measurement, a colloid sample was injected into a thin layer cell (0.5 to 1 mm in thickness) sandwiched by a polyethylene film, but the cell thickness was not controlled exactly. The sample was not relaxed enough to remove the shear force applied during the injection; its viscosity depended on the concentrations of NB and clay nanosheets. Thus, we do not discuss particle orientation based on the radial symmetry of the SAXS data.

CLSM Measurements. Some NB–Hect and NB–FH colloids were characterized by CLSM for observing colloidally dispersed nanosheets in real space. CLSM images were recorded on a Nikon Eclipse Ti-E inverted optical microscope equipped with a Nikon A1+ confocal laser scanning system by using an oil immersion objective lens (× 100). We separately observed NB and clay nanosheets in the binary colloids by recording scattering and fluorescence images. The former images were recorded by irradiating the sample with a 405-nm diode laser and detecting the scattered light of 400–750 nm from the sample without any cutoff filter. This technique essentially allows observation of all objects that can scatter the incident laser beam, resulting in detection of NB nanosheets (see Results section). The latter ones were obtained by irradiating the sample with a 488-nm Ar laser and detecting the light of 570–620 nm

through a color filter. This condition was employed for detecting clay nanosheets through observing fluorescence of a probe dye adsorbed on the nanosheets.

Selective observation of clay nanosheets with fluorescence CLSM images was enabled by selective adsorption a cationic fluorescence dye onto clay nanosheets. We have already reported this adsorption behavior; addition of cationic organic species into NB–clay binary nanosheet colloids cause selective adsorption of the organic molecules on clay nanosheets because of more hydrophobic nature of the clay nanosheet surfaces than those of NB nanosheets.[29] We employed rhodamine 6G (R6G) as the fluorescence probe, and the selective adsorption on clay nanosheets in the binary colloids is indicated by fluorescence spectra of R6G. Whereas R6G in a single-component NB nanosheet colloid shows a fluorescence maximum at a wavelength slightly blue-shifted position compared with the spectrum of an R6G aqueous solution, the dye in a binary colloid exhibits a fluorescent peak at the same position as that in a single-component clay nanosheets (Figure S1, Supporting Information). Thus, we added R6G to NB–clay binary colloids with the concentration of 5×10^{-5} mol L^{-1}.

RESULTS

Sample Appearance. All of the NB–clay binary colloids are milky turbid without no eye-detectable phase boundaries, as shown by digital camera images of Figure 1. The sample appearances are almost the same for all of the binary colloids. The homogeneous colloidal appearances were kept at least for a week. In addition, they show birefringence indicating liquid crystalline property from whole of the samples. These results indicate that NB and clay nanosheets in the binary colloids are mixed apparently homogeneously at a macroscopic scale, independent of the employed clay mineral species

although their particle sizes are different in two orders of magnitude.

The NB–clay binary colloids retain such macroscopic appearances for more than a few weeks. The stability depended on the sample composition and we did not follow the exact time lapse, and some samples showed macroscopic phase separation after several months. However, heterocoagulation was not observed. This is rationalized by negative surface charges of both NB and clay nanosheets; our preliminary zeta-potential measurement indicated –20 to –40 mV of NB nanosheets and negative surface charges of smectite-type clays have been well established by previous works.[43]

SAXS Analysis. We have employed SAXS measurements for detecting liquid crystalline ordering of nanosheet colloids. All of the nanosheet colloids examined in the present study show a power-law relationship $I(q) \propto q^{-2}$ where $I(q)$ is the scattering intensity and q is the magnitude of scattering vector, which is ascribed to the form factor scattering from isolated 2D particles, *i.e.*, nanosheets. The peaks due to nanosheet–nanosheet correlation, the structure factor, overlaps on the power-law scattering. To clearly discuss the structure factor, we plotted $I(q) \times q^2$ against q on log-log scales as shown in Figures 2–4 and Figures S1 and S2 (Supporting Information) of single-component NB and clay colloids and NB–clay binary colloids.

For single-component NB colloids, samples with the nanosheet concentrations higher than 40 g L^{-1} show scattering peaks although those with the concentration lower than 30 g L^{-1} do not show specific peaks (Figure 2A). The scattering observed for high concentration colloids is accompanied by higher-order peaks, indicating the presence of lamellar nanosheet ordering. The identification as "lamellar" phase will be discussed later. The basal spacings of the lamellar phases are several tens of nanometers as summarized in Table S1 (Supporting Information), indicating the formation of liquid crystalline phases.

In contrast, single-component clay colloids show different SAXS patterns depending on their lateral nanosheet size. Hect and Sapo colloids characterized by small lateral size (~ 30 nm) of clay nanosheets show only the $I(q) \sim q^{-2}$ relationship as indicated by the SAXS patterns lacking specific peaks (Figure 2B). FH and TSM colloids consisting of μm-size clay nanosheets exhibit the peaks due to lamellar liquid crystalline phase with the basal spacing of several tens of nanometers even at low nanosheet concentrations (> 10 g L^{-1}) (Figure 2C). These results are consistent with the previous reports on liquid crystallinity of NB and clay nanosheets.[23, 44]

On the other hand, all the NB–clay binary nanosheet colloids exhibit scattering peaks in their SAXS patterns; Figures 3 and 4 plots the SAXS patterns of the binary colloids with low and high NB concentrations of 10 and 40 g L^{-1}, respectively, and Figures S1 and S2 (Supporting Information) show the patterns with intermediate NB concentrations (20 and 30 g L^{-1}). They indicate the formation of lamellar phases at all of the examined NB concentrations of 10–40 g L^{-1} and clay concentrations of 5–40 g L^{-1}, irrespective of clay mineral species. Only one lamellar phase is found as the ordered phase in each sample even at the nanosheet concentrations where both NB and clay (FH and TSM) nanosheets can evolve ordered phases in their single-component colloids. We assign the lamellar phase found in the binary colloids to liquid crystalline ordering of NB nanosheets, as discussed later. Basal spacings of the lamellar phase are listed in Table S1 (Supporting Information). At fixed NB and clay concentrations, the spacings are generally larger for FH and TSM, characterized by larger nanosheet lateral seizes, than Hect and Sapo with smaller lateral sizes.

Basal spacing of the lamellar phase of NB–clay binary nanosheet colloids is related to the concentrations of both nanosheets. Figures 5 plots the basal spacing against

the clay nanosheet concentration at a fixed NB nanosheet concentration. Increase in the clay nanosheet concentration leads to decrease in the basal spacing, indicating compression of the lamellar phase of NB nanosheets by the introduction of clay nanosheets as discussed later. The dependency is apparently almost the same in the four NB–clay (Hect, Sapo, FH, or TSM) systems at the same niobate concentration, although FH and TSM give larger basal spacings, i.e., lesser extent of compression than Hect and Sapo. The basal spacing reduction with the clay concentration is steeper for low NB concentrations (10 and 20 g L^{-1}, Figures 5A and B).

In contrast, the basal spacing at a constant clay nanosheet concentration does not largely decrease with the increase of NB concentration. Figure 6 plots the basal spacing against the NB nanosheet concentration at each clay concentration. The double logarithmic plots are used for evaluating dimensionality of the swelling/compression of NB lamellar phase from the power law of $d \propto c_{NB}^{\beta}$, where d is the basal spacing and c_{NB} is the NB concentration. One- and three-dimensional swelling/compression is supposed from the exponent β of –1 and –1/3, respectively.[22, 24, 44] The β values estimated from Figure 6 are summarized in Table S2 (Supporting Information). Whereas β is around –1/3 for clay concentration, c_{clay}, of 5 g L^{-1}, the value is reduced with increasing c_{clay} to reach in the range of –0.01 to –0.1 at higher c_{clay}. In other words, the basal spacing is almost constant being independent of c_{NB} at higher c_{clay}.

Volume occupancy of the lamellar phase is estimated from its d value and the NB concentration c_{NB}, by assuming that the lamellar phase consists of NB nanosheets and all of the NB nanosheets are included in the ordered phase. The results are summarized in Table S1. The values being less than 100% evidence phase separation of the lamellar phase detected by SAXS from the other phase(s). At c_{NB} lower than 20 g L^{-1}, the volume

occupancy is generally smaller than 50%; the lamellar phase is a minor fraction in these colloids. However, it reaches 50% at c_{NB} and c_{clay} both larger than 30 g L^{-1}, and exceeds 90% at c_{NB} = 40 g L^{-1} and c_{clay} = 5 g L^{-1}.

CLSM Observations. We succeeded in separate detection of NB and clay nanosheets in the binary colloids by combining scattering and fluorescence observations of CLSM images. Scattering measurement detects NB nanosheets as red color but not clay (Lapo and FH) nanosheets, the results which would be ascribed to their higher electron density of NB nanosheets than clay nanosheets. In contrast, clay colloids are observed with fluorescence technique as green objects due to cationic R6G dye molecules adsorbed on clay nanosheets as probe dye.

Figure 7 shows CLSM images of single-component NB, Hect, and FH colloids measured with scattering and fluorescence techniques. CLSM image of a NB colloid (5 g L^{-1}) recorded by scattering method shows unevenly distributed red objects while the objects are broadly spread in the sample reflecting a colloidally dispersed state of the exfoliated nanosheets (Figure 7A). This image indicates localization, in other words concentration fluctuation, of NB nanosheets. On the other hand, fluorescence CLSM image of a Hect nanosheet colloid (5 g L^{-1}) exhibits homogeneous green color in whole of the sample, indicating spreading of clay nanosheets entirely in the colloid, reflecting infinite swelling of clay crystallites (Figure 7B). However, the fluorescence image of an FH nanosheet colloid (5 g L^{-1}) exhibits localized intense green color, indicating finite swelling of this clay mineral and inhomogeneous location of its nanosheets (Figure 7C). Scattering CLSM observations are not suitable to monitor Hect and FH nanosheets because clay particles are not detected as efficiently as those with the fluorescence observations.

CLSM images of a NB–Hect binary nanosheet colloid shown in Figure 8 give direct evidence for the phase-separation of NB and clay nanosheets in the colloid. Scattering observation of an NB–Hect binary colloid (concentrations of NB and Hect are both 10 and 5 g L^{-1}, respectively) exhibits inhomogeneous distribution of red objects as seen in the 3D image (Figure 8A). This indicates that NB nanosheets are distributed in the colloid as domains. The NB domains of around 5–20 μm length and around 5 μm thickness having irregular and scrambled but somewhat flat shapes are estimated from 3D and horizontal and vertical cross sectional 2D images shown in Figure 10 as well as Figure S3 (Supporting Information). Cross-sectional images (Figure 8B) apparently indicate the presence of aggregated platy particles in the domains. On the other hand, fluorescence CLSM observation indicates almost homogeneous distribution of Hect nanosheets as indicated by entire distribution of green color (Figure 8C). However, the horizontal cross section shows certain inhomogeneity of clay nanosheets distribution (Figure 8D). Superimposition of the horizontal 2D images of scattering (NB) and fluorescence (Hect) observations clarifies that voids among the NB nanosheets detected in the scattering image are filled with Hect nanosheets and vice versa (Figure 8E). This fact demonstrates spatial separation of NB and Hect nanosheets at a mesoscopic scale in real space.

A NB–FH binary nanosheet colloid with the same concentrations as those of the NB–Hect colloid also provides CLSM images showing phase separation (Figure 9). Scattering image indicates irregularly shaped domains of NB nanosheets similarly to that of NB–Hect colloid. FH nanosheets detected by fluorescence observation are not apparently homogeneously dispersed in whole of the colloid, being different from those in the NB–Hect binary colloid, but segregated in the sample to form intensely fluorescent

domains. Although some of FH nanosheets can be detected by scattering measurement as indicated by the observation of single FH nanosheet colloid (Figure 7), comparison of scattering and fluorescence images of the NB–FH colloid suggests that most of the objects detected by scattering observation are assigned to NB nanosheets. Superimposition of the images of NB nanosheets (scattering) and FH nanosheets (fluorescence) in the horizontal cross sections indicates spatially separated location of NB and FH nanosheets. This result is basically the same as that of the NB–Hect colloid. However, FH nanosheets are aggregated, or localized, to form their domains as evidenced by inhomogeneous green color of the fluorescence image, being in contrast to Hect nanosheets in the NB–Hect colloid.

Polarized optical microscope (POM) observations coincide with the CLSM results. POM images NB–Hect and NB–FH binary colloids shown in Figure S4 (Supporting Information) indicate the presence of discrete birefringent domains for both of the samples. The birefringent domains are assigned to the liquid crystalline NB nanosheet domains observed in the CLSM images based on their distribution and size. The images also support that clay nanosheets are non-birefringent, i.e., isotropic in the colloids.

DISCUSSION

Phase-Separation of NB–Clay Binary Nanosheet Colloids. SAXS and CLSM analysis of the NB–clay binary nanosheet colloids, where both of the nanosheets bear negative electric charges, indicate phase-separation of an ordered (liquid crystalline) and isotropic phases in the colloids. The ordered phases have lamellar structure with basal spacings of several tens of nanometers in all of the binary nanosheet colloids

independent of the employed clay minerals (Hect, Sapo, FH, and TSM). Nanosheet ordering in a lamellar fashion is rationalized by their 2D shape. Thus, we employ the term of lamellar phase for indicating the liquid crystalline ordering in the present paper. However, in the present study, we did not take care of accurately identifying the exact phase — nematic, lamellar, or columnar — but describe "lamellar" because all of these phases have "lamellar-like" ordering due to the 2D shape of nanosheets. Quantitative characterization using an upgraded instrument[45] will be a future problem.

Dependence of the basal spacings on the niobate or clay concentrations is essentially the same irrespective of the difference in clay minerals. Each sample contains one ordered phase. On the other hand, CLSM observations demonstrate spatial separation of niobate nanosheets and clay nanosheets in real space. Although distribution of clay nanosheets depends on the species (Hect or FH), that of niobate nanosheets is essentially the same.

From these results, we assign the ordered phase in the niobate–clay binary nanosheet colloids to lamellar liquid crystalline phase of niobate nanosheets. For single-component clay colloids, FH and TSM form liquid crystalline phases but Hect and Sapo only form isotropic phases. Great differences in the distribution between FH and Hect nanosheets are observed in both of the single-component and binary colloids, as demonstrated by CLSM. Nevertheless, all of clay minerals give essentially the same SAXS results after demixing with NB nanosheets, which cannot be rationalized if the lamellar phases in the binary colloids are induced by liquid crystalline ordering of clay nanosheets. Hence, we conclude that clay nanosheets are present in isotropic (disordered) states in all of the NB-clay binary colloids even though FH and TSM nanosheets themselves can form lamellar liquid crystalline phases in the absence of NB nanosheets.

NB nanosheets form ~10 μm size discrete domains which are spatially separated from clay nanosheets, directly indicating phase separation at a mesoscopic scale. NB nanosheets are aligned in a lamellar manner in each domain with a basal spacing of several tens of nanometers, which are seen in the CLSM images as aggregates of platy particles. The basal spacing and domain size suggest that each NB nanosheet domain contains several hundred to a thousand nanosheets.

The mesoscopic size of NB nanosheet domains in the binary colloids is ascribed to slow kinetics; the growth of NB nanosheet domains through Ostwald ripening[46] is suppressed in the presence of clay nanosheets, as viscous nature of clay colloids is widely known.[47] However, we suppose that the formation of lamellar structure detected by SAXS is completed even though the domain growth is suppressed. This idea is supported by the basal spacing and volume occupancy of the lamellar phase with different NB and clay concentrations being consistent each other. The volume occupancy approaching unity at high NB concentrations (Table S1, Supporting Information) indicates enough expansion of the distance between NB nanosheets in the binary colloids. Future works of long-term observations and rheological measurements, including detailed analyses of sol–gel behavior, of the samples are necessary to clarify the details.

Effects of Coexisting Clay Nanosheets on the Distribution of NB Nanosheets. The SAXS results indicate almost the same behavior of the lamellar phase of NB nanosheets for the four clay minerals examined in the present study; the basal spacing decreases as increasing the concentration of clay nanosheets at a constant NB concentration (Figure 5). This fact means compression of the domain volume of NB nanosheets in the presence of clay nanosheets. The same dependency of the basal spacings for different clay minerals shows that all of the clay minerals reduce the basal

spacing of the NB phase in the same manner as the increase of clay concentration. In contrast, the relationships of the basal spacing and NB nanosheet concentration (Figure 6) suggests three-dimensional compression/swelling of the liquid crystalline domains of niobate nanosheets for the lowest clay concentration examined (5 g L^{-1}) as evidenced by relationship between basal spacing d and NB concentration c_{NB}: $d \propto c_{NB}^{\beta}$, $\beta \sim -1/3$. However, the β value decreases with increasing c_{NB} to become close to 0, indicating almost constant basal spacing for a given clay concentration irrespective of the difference in c_{NB}. This behavior of the lamellar phase of NB nanosheets is not simply explained by compression induced by the coexisting isotropic clay phase.

We ascribe the constant basal spacing between the NB nanosheets at high clay concentrations to competition between the compressing force of the introduced clay phase and restoring force of the compressed NB phase. This is schematically illustrated in Figure 10. When concentrations of both NB and clay nanosheets are low, NB nanosheets in the lamellar phase are not crowded, and thus assembled with a large basal spacing. Introduction of clay nanosheets to this sample causes compression of the liquid crystalline domains of NB nanosheets (Figure 10a). Also, addition of NB nanosheets to this sample results in expansion of the NB domains but their basal spacing is somewhat reduced because the expansion of NB phase increases effective clay concentration (Figure 10b). In contrast, when the initial NB concentration is high, the NB domains are highly compressed. In this condition, effective clay concentration is also high. Addition of clay nanosheets to this sample does not compress the NB domains more and thus does not to reduce the basal spacing of liquid crystalline NB nanosheets (Figure 10c). Meanwhile, introduction of NB nanosheets to this sample does not reduce the basal spacing (Figure 10d).

Another possibility is contribution of clay nanosheets particles to osmotic swelling of niobate nanosheets. In the case of nanosheet colloids of $H_3Sb_3P_2O_{14}$, almost constant basal spacing against nanosheet concentration deviated from the one-dimensional swelling ($\beta \sim -1$ relationship) was observed at low nanosheet concentrations, and explained by expulsion of water from the liquid crystalline phase to the isotropic phase.[22] Although this system is a single-component one, being different from our binary colloids, water expulsion to the clay phase would occur to larger extent at high clay nanosheet concentrations because the clay phase requires larger amounts of water at higher particle concentrations for osmotic swelling of the clay phase.

On the other hand, absolute basal spacings of the lamellarly ordered NB nanosheets are larger for FH and TSM, which are characterized by nanosheet lateral lengths of micrometers, than for Hect and Sapo with the lateral lengths of several tens of nanometers. If we ascribe the phase separation to depletion of NB nanosheets by non-interacting clay nanosheets, the large size difference of clay nanosheets accompanied by a great difference in their excluded volume. Here, the size of FH and TSM nanosheets is comparable to that of NB nanosheets whereas Hect and Sapo nanosheets are much smaller than NB nanosheets. This leads to weaker depletion effects of FH and TSM than Hect and Sapo.[48] Smaller compression of the NB phase in the FH–NB and TSM–NB colloids qualitatively agree with such consideration. However, based on CLSM images, we suppose that the compression of NB phase is not simply explained by depletion. Although Hect nanosheets are distributed in whole of the colloid, FH nanosheets are localized or aggregated in the sample probably due to insufficient swelling due to the large particle size. The localized distribution of FH nanosheets permits larger volume occupancy of NB nanosheets in the colloid to give larger basal spacing.

CONCLUSIONS

In summary, the present study clarified particle distribution of niobate–clay binary inorganic nanosheets colloids, as the first experimental real-space observation of aqueous binary colloids of anisotropic particles. Although this system is apparently homogeneous at a macroscopic scale, niobate nanosheets form a lamellar liquid crystalline phase, which is separated from an isotropic phase of clay nanosheets. The lamellar phase is apparently compressed by the coexisting isotropic clay phase, as evidenced by shrinkage of the basal spacing of the lamellar structure; nevertheless, the lateral size of clay nanosheets little affects the basal spacing of the lamellar phase. Spatial separation of niobate and clay nanosheets are directly indicated by CLSM; niobate nanosheets form domains of similar shapes in the binary colloids and clay nanosheets are located in voids between the niobate domains. However, the distribution of clay nanosheets is greatly different with the employed clay mineral. The results demonstrate that the phase separation between niobate and clay nanosheets is not explained simply by depletion, indicating the importance of experimentally investigating real systems. Our results clearly describe mesoscopic hierarchical structures of niobate–clay binary nanosheet colloids in real space, and decoupling of domain structure of individual nanosheet species and final macroscopic structure constructed by assembling the nanosheet domains. They can be recognized as important fundamental knowledge for discovering unusual functions in multicomponent nanosheet colloids based on their multiscale dynamic structures.

ACKNOWLEDGMENTS

This work was partly supported by JSPS KAKENHI no. 18K04729 (for E.M.). This work was performed in part at the Queensland node of the Australian National Fabrication Facility Queensland Node (ANFF-Q), a company established under the National Collaborative Research Infrastructure Strategy to provide nano- and micro-fabrication facilities for Australia's researchers.

SUPPORTING INFORMATION

Figures of SAXS patterns of NB-clay binary nanosheet colloids at NB concentrations of 20 and 30 g L^{-1}, Table of basal spacings and volume occupancies of the NB lamellar for the binary nanosheet colloids, Table of the values of exponent β in the power low of $d \propto c_{NB}{}^{\beta}$ for the binary colloids, Figure of the cross-sectional images obtained by CLMS for (I) NB–Hect (10 g L^{-1} – 5 g L^{-1}) and (II) NB–FH (10 g L^{-1} – 5 g L^{-1}) binary colloids (PDF).

REFERENCES

(1) Mann, S., *Biomimetic Materials Chemistry*. Wiley-VCH: New York, 1996.

(2) Belmonte, M., Advanced Ceramic Materials for High Temperature Applications. *Adv. Eng. Mater.* **2006,** *8*, 693-703.

(3) René, C.; Turcotte, E., *Handbook of Material Science Research*. Nova Science Publishers: New York, 2010.

(4) Hamley, I. W., *Introduction to Soft Matter: Synthetic and Biological Self-Assembling Materials*. 2007; p 1-328.

(5) Niederberger, M., Multiscale Nanoparticle Assembly: From Particulate Precise Manufacturing to Colloidal Processing. *Adv. Funct. Mater.* **2017,** *27*, 1703647.

(6) Xu, T.; Gao, W.; Xu, L. P.; Zhang, X.; Wang, S., Fuel-Free Synthetic Micro-/Nanomachines. *Adv. Mater.* **2017,** *29*, 1603250.

(7) Asakura, S.; Oosawa, F., On Interaction between Two Bodies Immersed in a Solution of Macromolecules. *J. Chem. Phys.* **1954,** *22*, 1255-1256.

(8) Scheutjens, J. M. H. M.; Fleer, G. J., Interaction between Two Adsorbed Polymer Layers. *Macromolecules* **1985,** *18*, 1882-1900.

(9) Bailey, L.; Lekkerkerker, H. N. W.; Maitland, G. C., Smectite Clay - Inorganic Nanoparticle Mixed Suspensions: Phase Behaviour and Rheology. *Soft Matter* **2015,** *11*, 222-236.

(10) Onsager, L., The Effects of Shape on the Interaction of Colloidal Particles. *Ann. N. Y. Acad. Sci.* **1949,** *51*, 627-659.

(11) Gabriel, J.-C. P.; Davidson, P., Mineral Liquid Crystals from Self-Assembly of Anisotropic Nanosystems. *Top. Curr. Chem.* **2003,** *226*, 119-172.

(12) Stroobants, A.; Lekkerkerker, H. N. W., Liquid Crysta Transitions in a Solution of Rodlike and Disklike Particles. *J. Phys. Chem.* **1984,** *88*, 3669-3674.

(13) Bolhuis, P.; Frenkel, D., Numerical Study of the Phase Diagram of a Mixture of Spherical and Rodlike Colloids. *J. Chem. Phys.* **1994,** *101*, 9869-9875.

(14) Bates, M. A.; Frenkel, D., Phase Behavior of Model Mixtures of Colloidal Disks and Polymers. *Phys. Rev. E* **2000,** *62*, 5225-5229.

(15) Harnau, L.; Dietrich, S., Wetting and Capillary Nematization of Binary Hard-Platelet and Hard-Rod Fluids. *Phys. Rev. E* **2002,** *66*, 051702.

(16) Esztermann, A.; Reich, H.; Schmidt, M., Density Functional Theory for Colloidal Mixtures of Hard Platelets, Rods, and Spheres. *Phys. Rev. E* **2006,** *73*, 011409.

(17) Kleshchanok, D.; Meijer, J.-M.; Petukhov, A. V.; Portale, G.; Lekkerkerker, H.

N. W., Attractive Glass Formation in Aqueous Mixtures of Colloidal Gibbsite Platelets and Silica Spheres. *Soft Matter* **2011,** *7*, 2832.

(18) Woolston, P.; van Duijneveldt, J. S., Three-Phase Coexistence in Colloidal Rod-Plate Mixtures. *Langmuir* **2015,** *31*, 9290-9295.

(19) Chen, M.; He, M.; Lin, P.; Chen, Y.; Cheng, Z., Staged Phase Separation in the I-I-N Tri-Phase Region of Platelet-Sphere Mixtures. *Soft Matter* **2017,** *13*, 4457-4463.

(20) Pan, H.; Zhu, C.; Lu, T.; Lin, J.; Ma, J.; Zhang, D.; Zhu, S., A Chiral Smectic Structure Assembled from Nanosheets and Nanorods. *Chem. Commun.* **2017,** *53*, 1868-1871.

(21) Miyamoto, N.; Nakato, T., Liquid Crystalline Nature of $K_4Nb_6O_{17}$ Nanosheet Sols and Their Macroscopic Alignment. *Adv. Mater.* **2002,** *14*, 1267-1270.

(22) Gabriel, J.-C. P.; Camerel, F.; Lemaire, B. J.; Desvaux, H.; Davidson, P.; Batail, P., Swollen Liquid-Crystalline Lameller Phase Based on Extended Solid-Like Sheets. *Nature* **2001,** *413*, 504-508.

(23) Miyamoto, N.; Iijima, H.; Ohkubo, H.; Yamauchi, Y., Liquid Crystal Phases in the Aqueous Colloids of Size-Controlled Fluorinated Layered Clay Mineral Nanosheets. *Chem. Commun.* **2010,** *46*, 4166-4168.

(24) Michot, L. J.; Bihannic, I.; Maddi, S.; Funari, S. S.; Baravian, C.; Levitz, P.; Davidson, P., Liquid–Crystalline Aqueous Clay Suspensions. *Proc. Natl. Acad. Sci. USA* **2006,** *103*, 16101-16104.

(25) Xu, Z.; Gao, C., Aqueous Liquid Crystals of Graphene Oxide. *ACS Nano* **2011,** *5*, 2908-2915.

(26) Behabtu, N.; Lomeda, J. R.; Green, M. J.; Higginbotham, A. L.; Sinitskii, A.; Kosynkin, D. V.; Tsentalovich, D.; Parra-Vasquez, A. N. G.; Schmidt, J.; Kesselman,

E.; Cohen, Y.; Talmon, Y.; Tour, J. M.; Pasquali, M., Spontaneous High-Concentration Dispersions and Liquid Crystals of Graphene. *Nat. Nanotechnol.* **2010,** *5*, 406-411.

(27) Xia, Y.; Mathis, T. S.; Zhao, M. Q.; Anasori, B.; Dang, A.; Zhou, Z.; Cho, H.; Gogotsi, Y.; Yang, S., Thickness-Independent Capacitance of Vertically Aligned Liquid-Crystalline Mxenes. *Nature* **2018,** *557*, 409-412.

(28) Mejia, A.; Chang, Y.-W.; Ng, R.; Shuai, M.; Mannan, M.; Cheng, Z., Aspect Ratio and Polydispersity Dependence of Isotropic-Nematic Transition in Discotic Suspensions. *Phys. Rev. E* **2012,** *85*, 061708.

(29) Miyamoto, N.; Nakato, T., Liquid Crystalline Colloidal System Obtained by Mixing Niobate and Aluminosilicate Nanosheets: A Spectroscopic Study Using a Probe Dye. *Langmuir* **2003,** *19*, 8057-8064.

(30) Nakato, T.; Yamashita, Y.; Mouri, E.; Kuroda, K., Multiphase Coexistence and Destabilization of Liquid Crystalline Binary Nanosheet Colloids of Titanate and Clay. *Soft Matter* **2014,** *10*, 3161-3165.

(31) Pujala, R. K.; Pawar, N.; Bohidar, H. B., Universal Sol State Behavior and Gelation Kinetics in Mixed Clay Dispersions. *Langmuir* **2011,** *27*, 5193-203.

(32) Aliabadi, R.; Moradi, M.; Varga, S., Tracking Three-Phase Coexistences in Binary Mixtures of Hard Plates and Spheres. *J. Chem. Phys.* **2016,** *144*, 074902.

(33) van der Kooij, F. M.; Lekkerkerker, H. N. W., Liquid-Crystalline Phase Behavior of a Colloidal Rod-Plate Mixture. *Phys. Rev. Lett.* **2000,** *84*, 781-784.

(34) van der Kooij, F. M.; Vogel, M.; Lekkerkerker, H. N. W., Phase Behavior of a Mixture of Platelike Colloids and Nonadsorbing Polymer. *Phys. Rev. E* **2000,** *62*, 5397-5402.

(35) Adams, M.; Dogic, Z.; Keller, S. L.; Fraden, S., Entropically Driven Microphase

Transitions in Mixtures of Colloidal Rods and Spheres. *Nature* **1998,** *393*, 349-352.

(36) Koda, T.; Numajiri, M.; Ikeda, S., Smectic-a Phase of a Bidisperse System of Parallel Hard Rods and Hard Spheres. *J. Phys. Soc. Jpn.* **1996,** *65*, 3551-3556.

(37) Miyamoto, N.; Yamada, Y.; Koizumi, S.; Nakato, T., Extremely Stable Charge Separation in a Colloidal System Composed of Semiconducting Niobate and Clay Nanosheets. *Angew. Chem. Int. Ed.* **2007,** *46*, 4123-4127.

(38) Nakato, T.; Yamada, Y.; Miyamoto, N., Photoinduced Charge Separation in a Colloidal System of Exfoliated Layered Semiconductor Controlled by Coexisting Aluminosilicate Clay. *J. Phys. Chem. B* **2009,** *113*, 1323-1331.

(39) Nakato, T.; Inoue, S.; Hiraragi, Y.; Sugawara, J.; Mouri, E.; Aritani, H., Decomposition of a Cyanine Dye in Binary Nanosheet Colloids of Photocatalytically Active Niobate and Inert Clay. *J. Mater. Sci.* **2014,** *49*, 915-922.

(40) Nakato, T.; Terada, S.; Ishiku, T.; Abe, S.; Kamimura, S.; Mouri, E.; Ohno, T., Photoinduced Electron Transfer in Semiconductor–Clay Binary Nanosheet Colloids Controlled by Clay Particles as a Turnout Switch. *Appl. Catal. B* **2019,** *241*, 499-505.

(41) Levitz, P.; Lecolier, E.; Mourchid, A.; Delville, A.; Lyonnard, S., Liquid-Solid Transition of Laponite Suspensions at Very Low Ionic Strength: Long-Range Electrostatic Stabilization of Anisotropic Colloids. *Europhys. Lett.* **2000,** *49*, 672-677.

(42) Miyawaki, R.; Sano, T.; Ohashi, F.; Suzuki, M.; Kogure, T.; Okumura, T.; Kameda, J.; Umezome, T.; Sato, T.; Chino, D.; Hiroyama, K.; Yamada, H.; Tamura, K.; Morimoto, K.; Uehara, S.; Hatta, T., Some Reference Data for the Jcss Clay Specimens. *Nendo Kagaku (J. Clay Sci. Soc. Jpn.)* **2010,** *48*, 158-198 (in Japanese).

(43) Lagaly, G.; Dékány, I., Colloid Clay Science. In *Developments in Clay Science*, Bergaya, F.; Lagaly, G., Eds. Elsevier: 2013; Vol. 5, pp 243-345.

(44) Yamaguchi, D.; Miyamoto, N.; Fujita, T.; Nakato, T.; Koizumi, S.; Ohta, N.; Yagi, N.; Hashimoto, T., Aspect-Ratio-Dependent Phase Transitions and Concentration Fluctuations in Aqueous Colloidal Dispersions of Charged Platelike Particles. *Phys. Rev. E* **2012,** *85*, 011403.

(45) Davidson, P.; Penisson, C.; Constantin, D.; Gabriel, J. P., Isotropic, Nematic, and Lamellar Phases in Colloidal Suspensions of Nanosheets. *Proc. Natl. Acad. Sci. USA* **2018,** *115*, 6662-6667.

(46) Nakato, T.; Nono, Y.; Mouri, E.; Nakata, M., Panoscopic Organization of Anisotropic Colloidal Structures from Photofunctional Inorganic Nanosheet Liquid Crystals. *Phys. Chem. Chem. Phys.* **2014,** *16*, 955-62.

(47) van Olphen, H., *Clay Colloid Chemistry (Reprinted Edition)*. Krieger: Malabar, 1991.

(48) Tuinier, R.; Vliegenthart, G. A.; Lekkerkerker, H. N. W., Depletion Interaction between Spheres Immersed in a Solution of Ideal Polymer Chains. *J. Chem. Phys.* **2000,** *113*, 10768-10775.

Captions of Scheme and Figures

Scheme 1. Schematic Illustration of the Mesoscopic Architecture of NB–Clay Binary Nanosheet Colloids.

Figure 1. Photographs of (a) NB–Hect, (b) NB–Sapo, (c) NB–FH, (d) NB–TSM binary nanosheet colloids with the niobate and clay nanosheet concentrations of 20 g L^{-1}.

Figure 2. SAXS patterns of single-component NB and clay nanosheet colloids. Both axes are in log-scale. (A) Single-component NB nanosheet colloids of (a) 20, (b) 30, (c) 40, (d) 50, and (e) 60 g L^{-1}. (B) Single-component clay nanosheet colloids of (a) Hect 20, (b) Hect 30, (c) Sapo 20, and (d) Sapo 30 g L^{-1}. (C) Single-component clay nanosheet colloids of (a) FH 20, (b) TSM 20, (c) TSM 30, and (d) TSM 40 g L^{-1}.

Figure 3. SAXS patterns of NB–clay binary nanosheet colloids at NB concentration of 10 g L^{-1}. Both axes are in log-scale. (A) NB–Hect binary colloids with the clay concentration of (a) 5, (b) 10, (c) 20, (d) 30, and (e) 40 g L^{-1}. (B) NB–Sapo binary colloids with the clay concentration of (a) 5, (b) 10, (c) 20, and (d) 30 g L^{-1}. (C) NB–FH binary colloids with the clay concentration of (a) 5, (b) 10, (c) 20, (d) 30, and (e) 40 g L^{-1}. (D) NB–TSM binary colloids with the clay concentration of (a) 5, (b) 10, (c) 20, (d) 30, and (e) 40 g L^{-1}.

Figure 4. SAXS patterns of NB–clay binary nanosheet colloids at NB concentration of 40 g L^{-1}. Both axes are in log-scale. (A) NB–Hect binary colloids with the clay concentration of (a) 5, (b) 10, (c) 20, (d) 30, and (e) 40 g L^{-1}. (B) NB–Sapo binary colloids

with the clay concentration of (a) 5, (b) 10, (c) 20, (d) 30, and (e) 40 g L^{-1}. (C) NB–FH binary colloids with the clay concentration of (a) 5, (b) 10, (c) 20, (d) 30, and (e) 40 g L^{-1}. (D) NB–TSM binary colloids with the clay concentration of (a) 5, (b) 10, (c) 20, (d) 30, and (e) 40 g L^{-1}.

Figure 5. Basal spacings of the lamellar phase evolved in NB–clay binary colloids plotted against the clay nanosheet concentrations at constant niobate nanosheet concentration of (A) 10, (B) 20, (C) 30, and (D) 40 g L^{-1}.

Figure 6. Basal spacings of the lamellar phase evolved in NB–clay binary colloids plotted against the NB nanosheet concentrations at constant clay nanosheet concentration of (A) 5, (B) 10, (C) 20, (D) 30, and (E) 40 g L^{-1}.

Figure 7. 3D and cross-sectional images obtained by CLMS for (a) NB, (b) Hect, (c) FH nanosheet colloids. CLMS Images obtained by scattering mode and fluorescent mode are shown in red and green, respectively. Scanning areas (x-y plane) are fixed to 130 μm × 130 μm while the z-depth of the image is 100 μm for (a) NB and (b) Hect nanosheet colloids, and 90 μm for (c) FH nanosheet colloid. Cross-sectional images represents x-y cross sections at 50 mm z-depth. Cross-sectional images are contrast-adjusted.

Figure 8. 3D and cross-sectional images obtained by CLMS for NB-Hect (10 g L^{-1} – 5 g L^{-1}) binary nanosheet colloid. CLMS Images obtained by scattering mode and fluorescent mode are shown in red and green, respectively. 3D images (A, C) represent

visualized images of a 130 μm (x-length) × 130 μm (y-length) × 100 μm (z-depth) volume for each mode. Cross-sectional images (B, D) represents x-y cross sections at 50 μm z-depth. Superimposed image (E) is created by the integration of the images obtained by the two modes. Cross-sectional images are contrast-adjusted.

Figure 9. 3D and cross-sectional images obtained by CLMS for NB–FH (10 g L^{-1} – 5 g L^{-1}) binary nanosheet colloid. CLMS Images obtained by scattering mode and fluorescent mode are shown in red and green, respectively. 3D images (A, C) represent visualized images of a 130 μm (x-length) × 130 μm (y-length) × 100 μm (z-depth) volume for each mode. Cross-sectional images (B, D) represents x-y cross sections at 50 μm z-depth. Superimposed image (E) is created by the integration of the images obtained by the two modes. Cross-sectional images are contrast-adjusted.

Figure 10. Schematic representation of the competition between the compressing force of the introduced clay phase and restoring force of the compressed NB phase in the phase-separated binary colloids of NB and clay nanosheets.

Abstract graphic

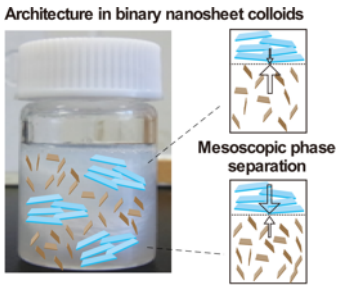

Scheme and Figures

Scheme 1. Schematic Illustration of the Mesoscopic Architecture of NB–Clay Binary Nanosheet Colloids.

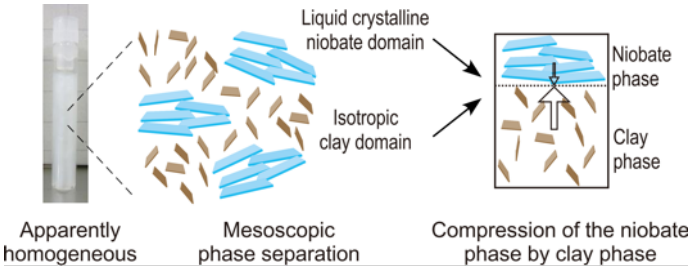

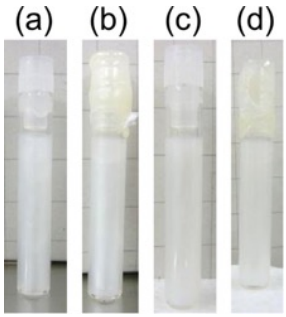

Figure 1. Photographs of (a) NB–Hect, (b) NB–Sapo, (c) NB–FH, (d) NB–TSM binary nanosheet colloids with the niobate and clay nanosheet concentrations of 20 g L^{-1}.

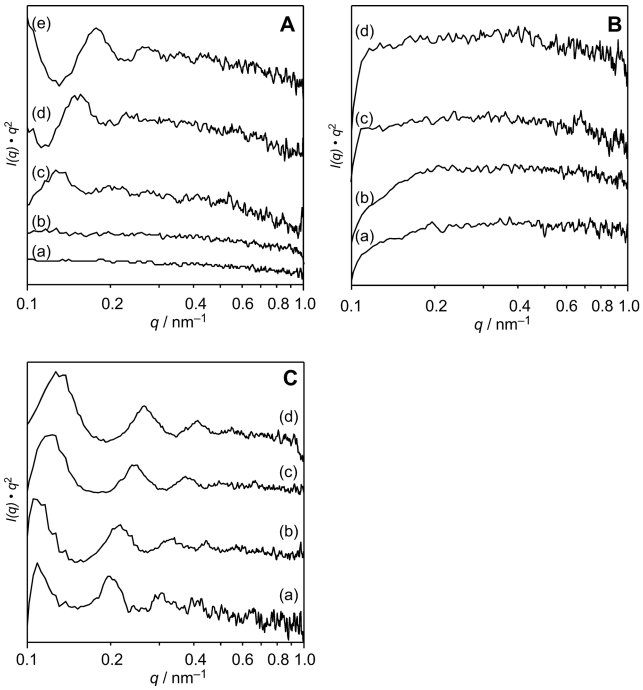

Figure 2. SAXS patterns of single-component NB and clay nanosheet colloids. Both axes are in log-scale. (A) Single-component NB nanosheet colloids of (a) 20, (b) 30, (c) 40, (d) 50, and (e) 60 g L^{-1}. (B) Single-component clay nanosheet colloids of (a) Hect 20, (b) Hect 30, (c) Sapo 20, and (d) Sapo 30 g L^{-1}. (C) Single-component clay nanosheet colloids of (a) FH 20, (b) TSM 20, (c) TSM 30, and (d) TSM 40 g L^{-1}.

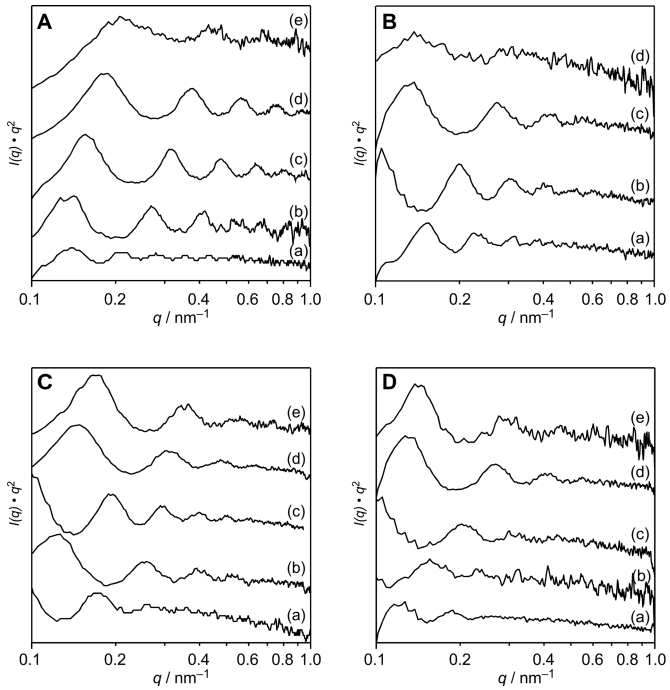

Figure 3. SAXS patterns of NB–clay binary nanosheet colloids at NB concentration of 10 g L^{-1}. Both axes are in log-scale. (A) NB–Hect binary colloids with the clay concentration of (a) 5, (b) 10, (c) 20, (d) 30, and (e) 40 g L^{-1}. (B) NB–Sapo binary colloids with the clay concentration of (a) 5, (b) 10, (c) 20, and (d) 30 g L^{-1}. (C) NB–FH binary colloids with the clay concentration of (a) 5, (b) 10, (c) 20, (d) 30, and (e) 40 g L^{-1}. (D) NB–TSM binary colloids with the clay concentration of (a) 5, (b) 10, (c) 20, (d) 30, and (e) 40 g L^{-1}.

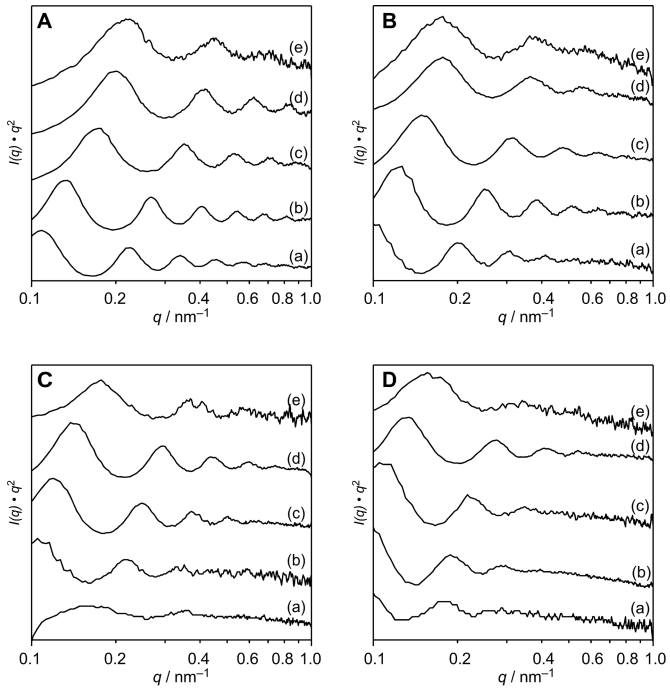

Figure 4. SAXS patterns of NB–clay binary nanosheet colloids at NB concentration of 40 g L^{-1}. Both axes are in log-scale. (A) NB–Hect binary colloids with the clay concentration of (a) 5, (b) 10, (c) 20, (d) 30, and (e) 40 g L^{-1}. (B) NB–Sapo binary colloids with the clay concentration of (a) 5, (b) 10, (c) 20, (d) 30, and (e) 40 g L^{-1}. (C) NB–FH binary colloids with the clay concentration of (a) 5, (b) 10, (c) 20, (d) 30, and (e) 40 g L^{-1}. (D) NB–TSM binary colloids with the clay concentration of (a) 5, (b) 10, (c) 20, (d) 30, and (e) 40 g L^{-1}.

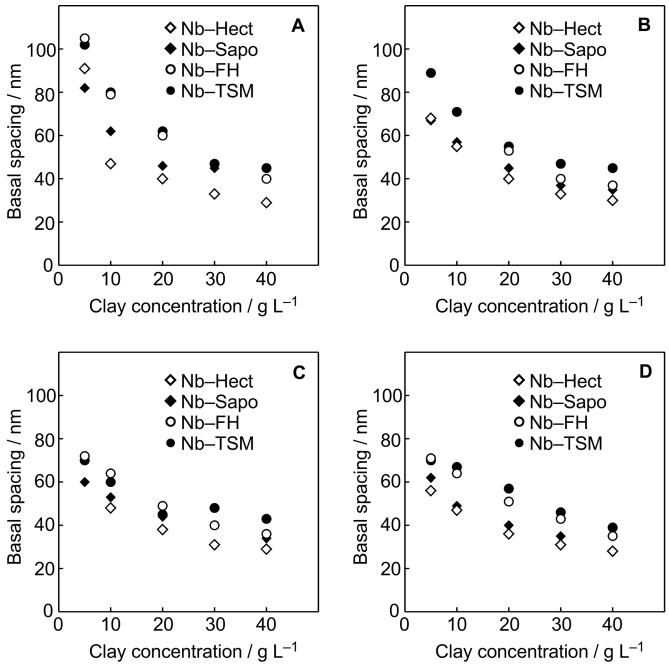

Figure 5. Basal spacings of the lamellar phase evolved in NB–clay binary colloids plotted against the clay nanosheet concentrations at constant niobate nanosheet concentration of (A) 10, (B) 20, (C) 30, and (D) 40 g L^{-1}.

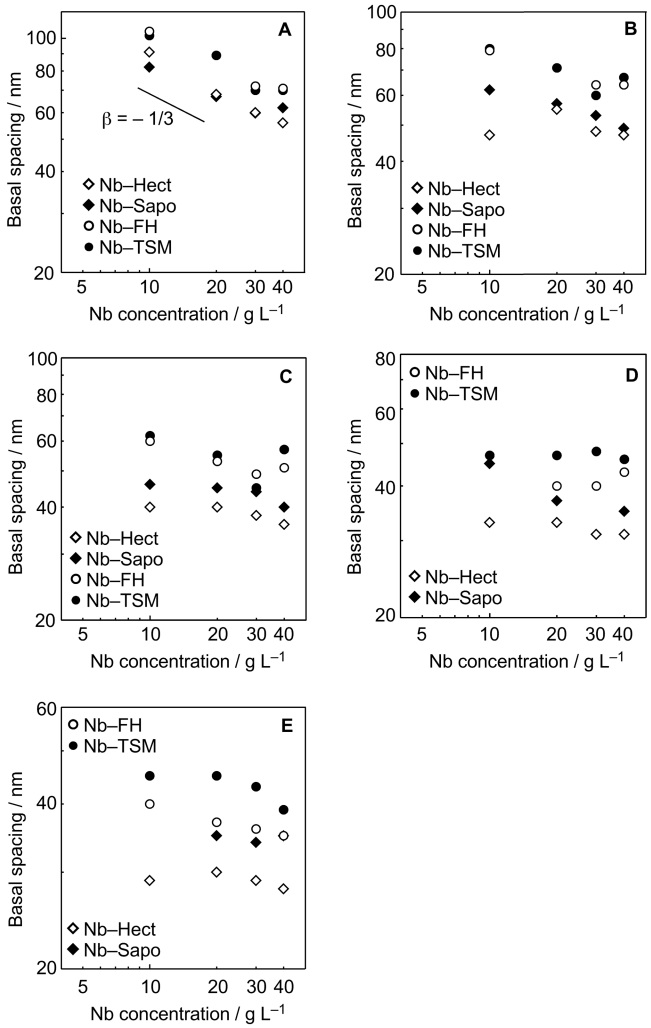

Figure 6. Basal spacings of the lamellar phase evolved in NB–clay binary colloids plotted against the NB nanosheet concentrations at constant clay nanosheet concentration of (A) 5, (B) 10, (C) 20, (D) 30, and (E) 40 g L^{-1}.

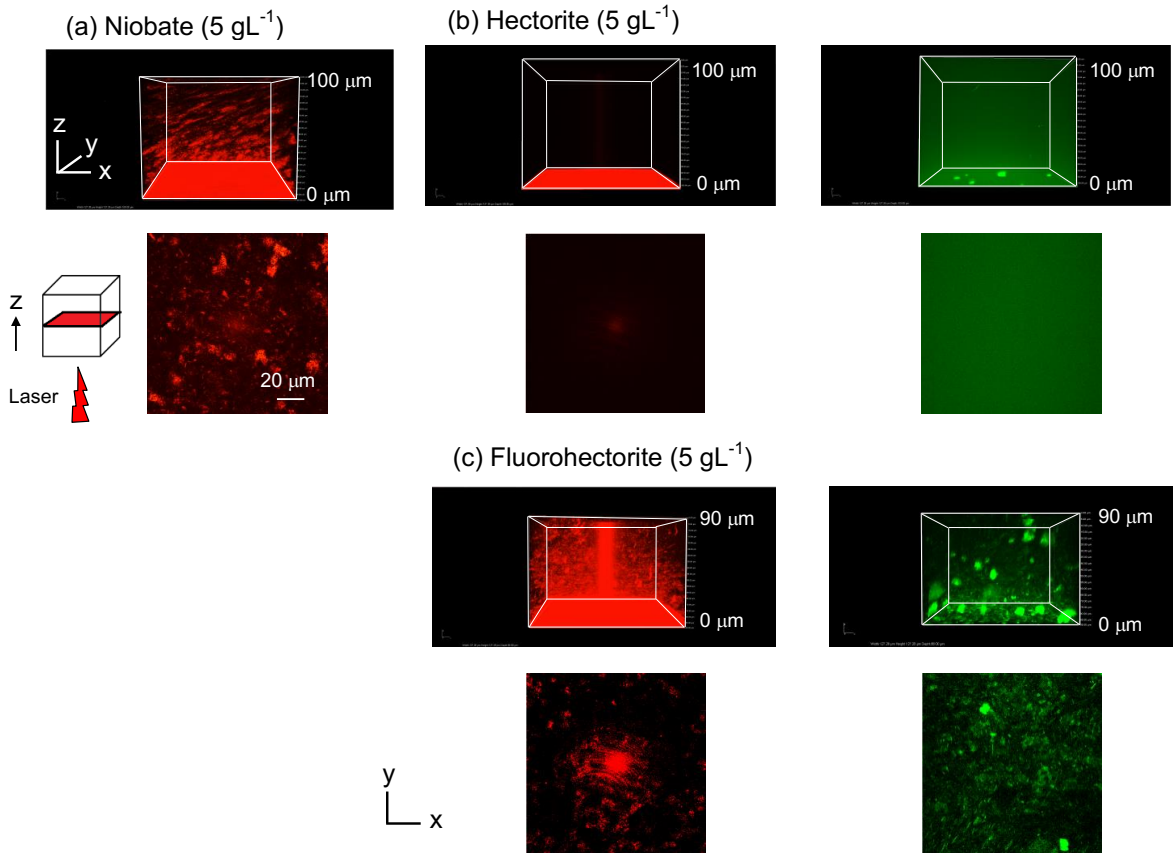

Figure 7. 3D and cross-sectional images obtained by CLMS for (a) NB, (b) Hect, (c) FH nanosheet colloids. CLMS Images obtained by scattering mode and fluorescent mode are shown in red and green, respectively. Scanning areas (x-y plane) are fixed to 130 μm × 130 μm while the z-depth of the image is 100 μm for (a) NB and (b) Hect nanosheet colloids, and 90 μm for (c) FH nanosheet colloid. Cross-sectional images represents x-y cross sections at 50 mm z-depth. Cross-sectional images are contrast-adjusted.

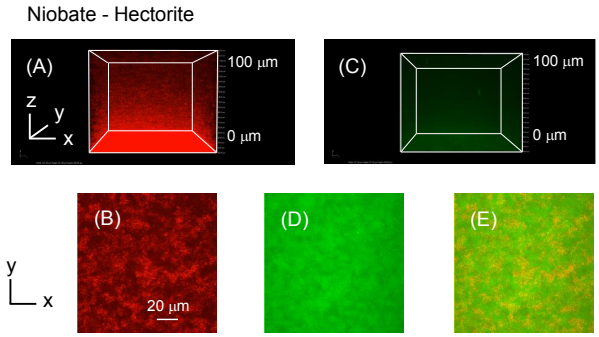

Figure 8. 3D and cross-sectional images obtained by CLMS for NB-Hect (10 g L^{-1} – 5 g L^{-1}) binary nanosheet colloid. CLMS Images obtained by scattering mode and fluorescent mode are shown in red and green, respectively. 3D images (A, C) represent visualized images of a 130 μm (x-length) × 130 μm (y-length) × 100 μm (z-depth) volume for each mode. Cross-sectional images (B, D) represents x-y cross sections at 50 μm z-depth. Superimposed image (E) is created by the integration of the images obtained by the two modes. Cross-sectional images are contrast-adjusted.

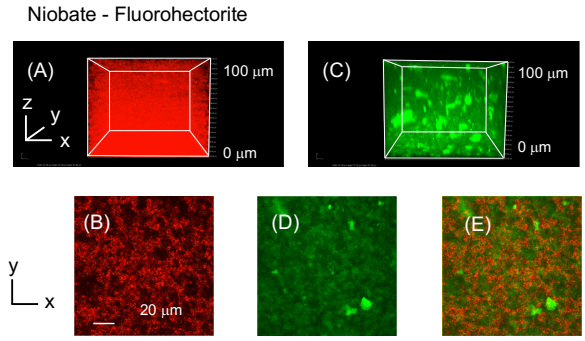

Figure 9. 3D and cross-sectional images obtained by CLMS for NB–FH (10 g L^{-1} – 5 g L^{-1}) binary nanosheet colloid. CLMS Images obtained by scattering mode and fluorescent mode are shown in red and green, respectively. 3D images (A, C) represent visualized images of a 130 μm (x-length) × 130 μm (y-length) × 100 μm (z-depth) volume for each mode. Cross-sectional images (B, D) represents x-y cross sections at 50 μm z-depth. Superimposed image (E) is created by the integration of the images obtained by the two modes. Cross-sectional images are contrast-adjusted.

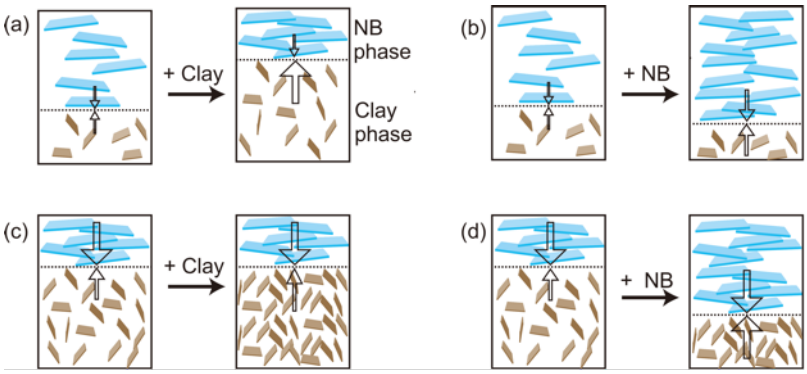

Figure 10. Schematic representation of the competition between the compressing force of the introduced clay phase and restoring force of the compressed NB phase in the phase-separated binary colloids of NB and clay nanosheets.